



Metal-like peak stress behavior of yttrium-doped BaCeO₃ ceramic

M. Jiménez-Melendo^{a,*}, C. Jiménez-Holgado^b

^a Departamento de Física de la Materia Condensada, Universidad de Sevilla, 41080 Sevilla, Spain

^b Departamento de Química Orgánica y Química Inorgánica, Facultad de Ciencias, Universidad de Alcalá de Henares, 28805 Alcalá de Henares, Spain

ARTICLE INFO

Keywords:

Perovskites

Creep

Microstructure-final

Twinning

ABSTRACT

The high-temperature mechanical behavior of polycrystalline 5 at% yttrium-doped barium cerate with sub-micronic grain size ($d = 0.5 \mu\text{m}$) has been studied in compression between 1200 and 1300 °C at different initial strain rates. The true stress – strain curves display an initial peak stress followed by a softening stage and then by an extended steady-state stage; the magnitude of the peak stress is strongly dependent on strain rate and temperature. These characteristics are very similar to those found in metals and metallic alloys that exhibit dynamic recrystallization during creep at elevated temperatures. Microstructural observations by scanning and transmission electron microscopy have shown that the grain structure is progressively refined with increasing strain due to the strong interaction between dislocations and pre-existing twin boundaries, originated by the various crystal transformations that occur upon cooling from the sintering temperature. The empirical equations used in metals to describe the relationship between strain rate, peak stress, and peak strain are also valid in the present ceramic material.

1. Introduction

The flow behavior at high temperatures ($T > T_m$, where T_m is the melting temperature) of polycrystalline materials involves complex processes such as grain boundary sliding, dislocation glide and climb, mass transport, etc. In metals and metallic alloys, dynamic recrystallization (DRX) strongly affects their creep behavior due to the softening and enhancement of ductility associated with the reconstruction of the microstructure [1–14]: new, smaller grains appear, resulting in an initial drop in stress with strain. The magnitude of the stress drop depends on the deformation conditions, mainly temperature and strain rate. In low- and moderate-stacking fault energy (SFE) metals (Ni, Ti, Mg, austenitic Fe, etc.), DRX is usually triggered by the nucleation and growth of new grains by grain boundary migration (usually called discontinuous recrystallization). In contrast, in high SFE metals (aluminum, β -titanium alloys, ferritic steels, etc.), the new grains are formed by the progressive transformation of dislocation sub-boundaries (low-angle boundaries) formed during the hardening stage into high-angle grain boundaries (continuous recrystallization). After the softening stage, a steady state of deformation is attained corresponding to the new grain size distribution. Depending on the characteristics of the material and the deformation conditions, the material can undergo additional refinement cycles, resulting in multiple stress peak behavior. Continuous DRX has also been

found in important mineral phases such as olivine $\text{Mg}_{0.9}\text{Fe}_{0.1}\text{SiO}_4$ [15, 16], the primary component of the upper mantle of the Earth, calcite CaCO_3 [17], NaNO_3 [18] and quartz [19,20], as well as in other ceramic materials such as NaCl [21] and LiF [22].

It has been reported [23,24] that the high-temperature plastic deformation of trivalent cation-doped (Y and Yb) barium cerates with submicronic grain sizes in the ductile regime is characterized by true stress σ - true strain ϵ curves exhibiting a broad peak stress in the early stages of deformation followed by a softening regime and then by an extended steady state. The magnitude and strain position of the peak stress are strain rate- and temperature-dependent, being more evident (relative to the steady-state flow stress) at lower temperatures and higher strain rates. This behavior, not observed previously in other fine-grained ceramics, is phenomenologically identical to that noted above for metals and metallic alloys that exhibit DRX at warm and hot working conditions.

Barium cerate is a perovskite-structured oxide used in the field of electrochemical energetics, particularly as an electrolyte in solid oxide fuel cells, due to its highly proton electrical conductivity [25,26]. Substitution of Ce^{4+} -site by trivalent ions (such as Y, Yb, Nd, and Gd) causes the formation of oxygen vacancies, which allow for protonic conduction upon exposure to water vapor at relatively elevated temperatures. The high-temperature mechanical properties of this solid-state proton

* Corresponding author.

E-mail address: melendo@us.es (M. Jiménez-Melendo).

<https://doi.org/10.1016/j.jeurceramsoc.2022.03.002>

Received 9 November 2021; Received in revised form 1 March 2022; Accepted 2 March 2022

Available online 4 March 2022

0955-2219/© 2022 The Author(s). Published by Elsevier Ltd. This is an open access article under the CC BY-NC-ND license (<http://creativecommons.org/licenses/by-nc-nd/4.0/>).

conductor are therefore of special relevance in the design of solid oxide fuel cells and other high-temperature operating devices because under working conditions, deformation, softening, mechanical degradation, and failure determine the behavior and performance of the material. In addition, high-temperature plastic deformation is usually controlled by diffusion and can thus provide basic information about mass transport in materials where no diffusion measurements have been undertaken. Other kinetic processes such as sintering, sinter-forging, grain growth, solid-state reaction, etc., are also governed by diffusion in ultimate instance, and such information can be thus used to devise optimum processing schedules.

No conclusive explanation on the origin of the metal-like stress drop behavior during the creep of fine-grained barium cerate has yet been presented. Therefore, the objective of this work was to investigate more deeply the occurrence of the peak stress and subsequent softening and steady-state stages during the high-temperature plastic deformation of this perovskite, in order to assess the mechanisms responsible for such a behavior. To this end, mechanical tests have been carried out under selected deformation conditions and correlated with detailed observations by scanning and, particularly, transmission electron microscopy, which have revealed the occurrence of extensive twinning in the as-received material. Studies on phase transformation on BaCeO₃ [27,28] have shown that this perovskite is prone to twinning owing to the various crystal transformations that occur upon cooling from the sintering temperature. Although with some discrepancies, it has been reported [25,29,30] that BaCeO₃ undertakes at least three phase transitions: a second-order transition from orthorhombic Pnma (perovskite structure) to orthorhombic Incn at 290–300 °C, a first-order transition from Incn to rhombohedral structure R-3c at 400 °C, and finally a second-order phase from rhombohedral to cubic Pm-3m at 839–880 °C. The transformation of a crystal phase in another of lower symmetry with different orientational variants (as in the present case) inevitably gives rise to twinning. Such phase-transformation-induced twinning has also been observed in many other perovskite oxides, such as CaTiO₃, MgSiO₃, LaGaO₃, LaMnO₃, BaTiO₃, etc. [31–35]. The deformation mechanisms responsible for the peak stress behavior in BaCeO₃ are discussed in relation to the interaction between dislocations and these pre-existing phase transformation-mediated twin boundaries.

2. Materials and experimental methods

Polycrystalline BaCe_{0.95}Y_{0.05}O_{2.975} (5Y-BCO) with a final density of 95 ± 1% (relative to the theoretical density $\rho = 6360 \text{ kg/m}^3$ of BaCeO₃) was produced using a solid-state reaction route described elsewhere [23, 24]. Briefly, BaCO₃, CeO₂, and Y₂O₃ powders (Sigma-Aldrich, purity > 99.0%) were mixed in the required stoichiometric ratio and ground. The resulting powder was calcined for 10 h at 1200 °C in air and reground again. Pellets were obtained by uniaxial pressing at 150 MPa followed by cold isostatic pressing at 210 MPa, and then sintered in air at 1550 °C for 10 h. It has been reported that sintering temperatures above 1600 °C produce barium evaporation and consequently the formation of CeO₂ precipitates [36,37], while lower temperatures result in poor densification. A sintering temperature of 1550 °C was then selected to produce the highest density material without compromising the perovskite crystal structure.

The structural analysis of the crystalline phases in both the calcined powders and sintered polycrystals was performed by using a Bruker AXS Advance D2 diffractometer in Bragg-Brentano configuration with Cu-K α radiation (X-Ray Laboratory, CITIUS, University of Sevilla, Spain). Data were collected in the 2 θ region between 20° and 70° with a step size of 0.02° and 10 s/step of acquisition. X-ray spectra were processed by the Le Bail refinement method using the TOPAS 4.2 Bruker AXS software package.

Specimens of 5 × 3 × 3 mm in size were cut from the sintered pellets and used for mechanical testing. Compressive tests were performed at temperatures T between 1200 and 1300 °C (0.73–0.78 T_m, where T_m =

2016 K = 1743 °C is the melting temperature of BaCeO₃ [38]) at constant cross-head speed and at constant load under selected conditions for which the peak stress behavior was clearly observed. Data were analyzed using the standard high-temperature power law for steady-state deformation [39–41]:

$$\dot{\epsilon} = A \sigma^n d^{-p} \exp(-Q/RT) \quad (1)$$

where A is a parameter depending on the deformation mechanism, d is the grain size, n is the stress exponent, p is the grain size exponent, Q is the activation energy for flow and R is the gas constant.

The microstructural characterization of as-fabricated and deformed polycrystals was carried out using scanning (SEM) and transmission (TEM) electron microscopy. To reveal grain boundaries, longitudinal sections were cut from the samples and mechanically polished using up to 0.25 μm -grade diamond paste, and then thermally etched at 1150 °C for 2 h in air. The relevant morphological parameters, grain size d (taken as the equivalent planar diameter), form factor F, and preferential orientation angle W were measured from SEM micrographs using a semiautomatic image analyzer (ImageJ software) averaging over more than 500 grains. Thin films for TEM observations were obtained from the as-fabricated and deformed samples following a classical procedure of grinding and ion-thinning until electron transparency.

3. Results

3.1. Crystal structure

Fig. 1 shows the X-ray diffraction pattern of a sintered 5Y-BCO polycrystal, confirming the presence of the single perovskite phase with space group Pnma: the peak positions correspond to the orthorhombic structure of undoped BaCeO₃ (ICDD PDF-2 card No. 04-006-1225). Within the resolution of XRD, no additional phases, in particular CeO₂ (PDF-2 card No. 01-078-5328), were observed. The lattice parameters calculated using the Le Bail refinement method are a = 6.238 Å, b = 8.769 Å and c = 6.252 Å, which are within the range of values reported for trivalent cation-doped barium cerate perovskites [24,25].

3.2. Initial microstructure

Fig. 2(a) shows the microstructure of as-prepared 5Y-BCO. It is formed by fine and equiaxed grains with a form factor of F = 0.82, indicating a regular grain growth during sintering without preferential grain orientation. The corresponding grain size distribution (Fig. 2(b)) is consistent with a lognormal law, as usually found in ceramics; the average grain size and the standard deviation of the lognormal distribution are $d = 0.55 \pm 0.25 \mu\text{m}$. This submicronic size contrasts strongly with the value of $d \simeq 4 \mu\text{m}$ measured in undoped barium cerate fabricated by the same procedure, indicating that yttrium doping dramatically increases the resistance to grain coarsening of the perovskite. A similar trend has been reported in other cation-doped ceramics such as yttrium- and zirconium-doped alumina [42,43], yttrium-stabilized tetragonal zirconia [44], yttrium-doped barium zirconate [45] and other perovskite oxides for solid oxide fuel cells [46]. This effect has been attributed to the segregation of dopant cations along the grain boundaries, which inhibits, or at least slows down, the grain boundary diffusivity relative to pristine materials.

The internal grain structure was investigated by TEM (Fig. 3). The grains are well-faceted and equiaxed, free of dislocations, and without secondary phases along the boundaries and triple grain junctions. The most notably defect in the grain structure is the presence of numerous contrast lines corresponding to twin boundaries, homogeneously distributed in the volume of the material. Fig. 3 shows representative images of these intragranular domains, with the boundaries extending across the grains or intersecting with each other. As noted in the

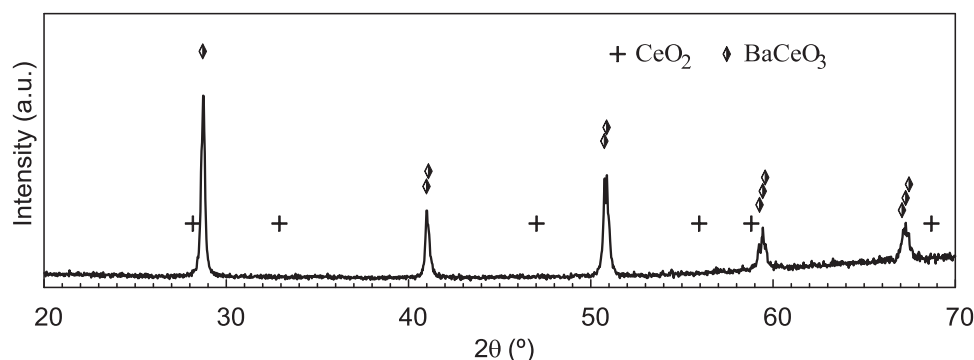


Fig. 1. X-ray diffractogram of sintered 5 at% Y-doped BaCeO₃ polycrystal. Peak positions for orthorhombic BaCeO₃ and cubic CeO₂ are shown (ICDD PDF-2 cards No. 04-006-1225 and 01-078-5328, respectively).

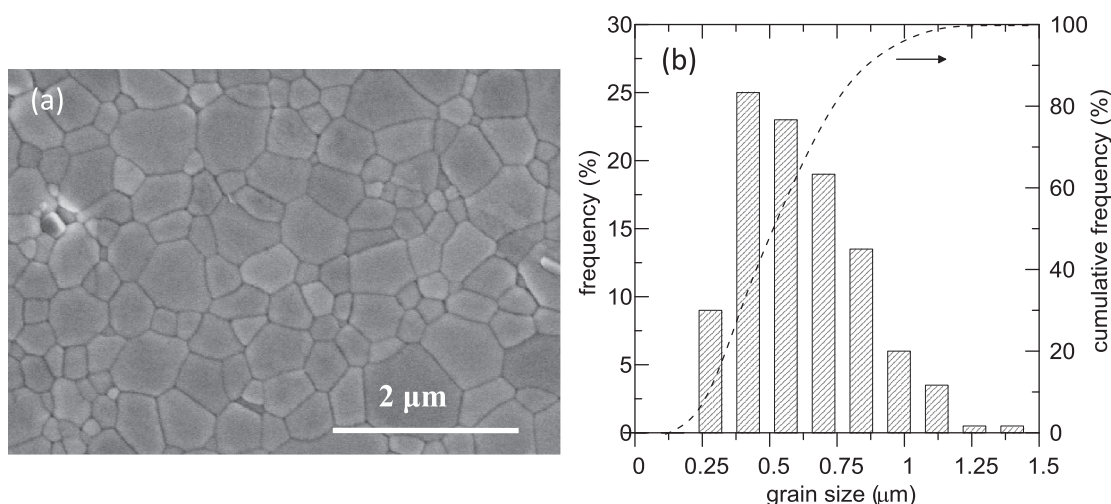


Fig. 2. (a) Microstructure of as-sintered 5 at% Y-doped BaCeO₃. (b) Corresponding grain size distribution.

Introduction, BaCeO₃ and other perovskite oxides [27,28,31–35] exhibit extensive phase transformation-induced twinning owing to the various changes in crystal structure that occur upon cooling from the sintering temperature. Cheng et al. [27,28] conducted detailed TEM studies on undoped and 10 at% Y- and 10 at% Nd-doped barium cerate fabricated following a procedure similar to that used in the present study (sintering for 2 h at 1400 °C, relative density of 76%). The authors reported a phase transformation-induced microstructure very similar to that observed in the present material, formed predominantly by reflection twins on the {110} and {112} planes. The same domain morphology has been reported in other perovskite oxides, such as CaTiO₃ [31] and LaGaO₃ [33].

3.3. Deformation tests

Fig. 4(a) displays the true stress σ - true strain ε curves of samples compressed at 1250 °C and different initial strain rates $\dot{\varepsilon}_0$. They exhibit an unusual behavior compared to other ceramics; for the sake of comparison, the σ - ε curve for 3 mol% yttria-stabilized tetragonal zirconia (3YTZP, the reference material for superplastic ceramics) with $d = 0.5 \mu\text{m}$ is also shown in Fig. 4(a) (dotted line).

The main characteristics of these curves are: (i) After the elastic part, there is a short hardening stage before reaching a maximum stress σ_p at a strain level ε_p (stage I in Fig. 4(b)); (ii) The magnitude of both the peak stress σ_p and the peak strain ε_p increases with increasing the initial strain rate and/or decreasing the temperature; (iii) After the peak stress, there is a softening stage where the flow stress decreases smoothly until a minimum stress σ_{ss} is reached (stage II); (iv) This stress σ_{ss} marks the

onset of an extended steady state of deformation (stage III), characterized by a positive slope of the σ - ε curves due to the continuously increase in true strain rate during a compressive constant cross-head speed test; and (v) The magnitude of the stress drop $\Delta\sigma$ (defined as the difference between the maximum stress σ_p and the steady-state flow stress extrapolated to ε_p to avoid the effect of softening, Fig. 4(b)) is practically constant, with a value of 1.5 ± 0.1 . This result suggests that the mechanism responsible for softening is the same regardless of the test conditions.

Reports of the occurrence of an initial decrease in flow stress during steady-state deformation in ceramics are very scarce and definitely different in shape. Sharp yield drops have been reported in fine-grained tetragonal ZrO₂-30 vol% spinel composite [47] and in large-grained MgO [48] and TiC [49], which were attributed to multiplication of dislocations in the volume of the grains in the early stages of creep. This mechanism, identical to that observed in well-grown single crystals with very low initial dislocation densities (sigmoidal creep) [41], results in rather sharp stress drops which are little affected by strain rate, contrary to the rounded stress peaks found in the present work, which are strongly dependent on strain rate and temperature.

The features listed above are however typical of metallic materials that exhibit DRX during deformation [1–14], as illustrated in Fig. 5 for a 42CrMo steel deformed at temperatures between 800 and 1200 °C (0.64 – 0.87 of the homologous temperature). In these materials, the peak stress, the softening stage, and the subsequent steady-state flow result from a dynamic balance between dislocation work hardening, dislocation recovery (usually by climb) and DRX, which leads to a refinement of the average grain size of the material before attaining the steady state.

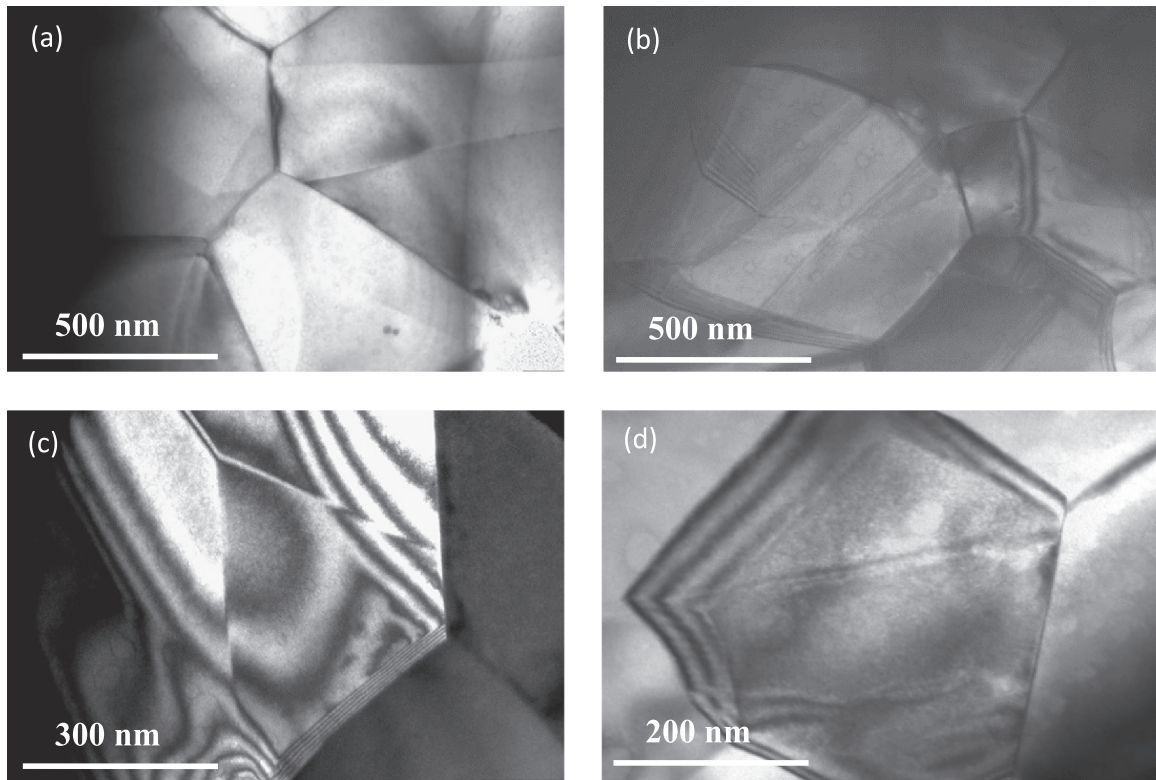


Fig. 3. TEM images of as-sintered 5Y-BCO under different diffraction conditions. Phase transformation-induced twin boundaries were commonly observed, usually extending across grain boundaries but also intersecting each other. No dislocation activity was observed in the grains.

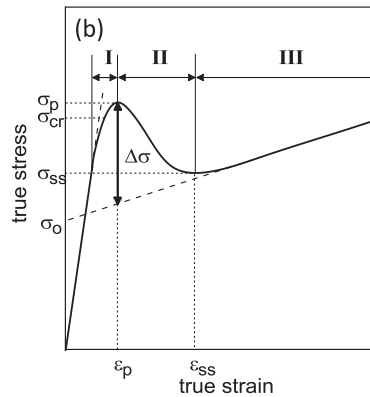
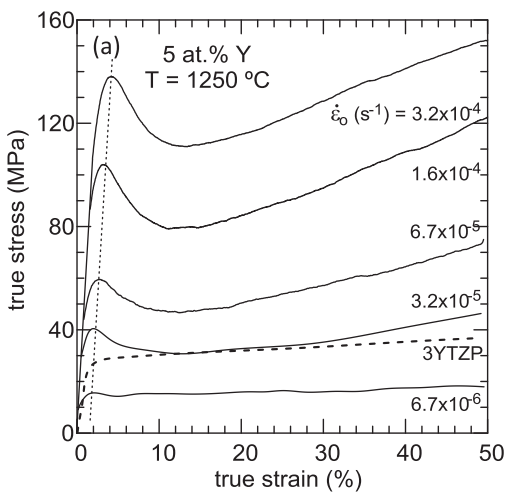


Fig. 4. (a) Variation of the flow stress with strain in 5Y-BCO at 1250 °C and various initial strain rates, showing a peak stress behavior similar to that of metals with dynamic recrystallization. For clarity, a schematic diagram of the stress – strain curve is displayed in (b), showing the three observed stages: I – hardening, II – softening, and III – steady state, and the characteristic magnitudes of stress and strain. The deformation curve for fine-grained 3YTZP ($d = 0.5 \mu\text{m}$) at $2 \times 10^{-5} \text{s}^{-1}$ is shown in (a) for comparison (dotted line).

The slopes of the $\sigma - \epsilon$ curves in Fig. 5 are nearly zero due to the use of true constant strain rate tests. It should be noted however that the initial grain size in metals is usually several tenths of micrometers, compared to the submicronic size of the current material.

The appearance of a softening stage prior to steady state in the present perovskite has also been verified by creep tests performed at constant load, as shown in Fig. 6 for a sample deformed at 1265 °C and at an initial stress of 22 MPa. Upon loading, the strain rate raises smoothly (softening stage) until a maximum is attained (the onset of the steady state) and thus decreases monotonically with a constant negative slope (due to the continuous increase in specimen section with strain in compressive constant load tests).

3.4. Microstructure of deformation

Fig. 7 shows SEM images of three samples tested at identical conditions of strain rate and temperature but voluntarily ended at different strain levels of 4%, 8% and 50%, corresponding to the typical regions observed in the stress – strain curves (Fig. 4): peak stress, softening stage and after prolonged steady-state deformation, respectively. Regardless of the final strain, the grains remain equiaxed with an average form factor F essentially unaffected by the creep process, indicating that grain boundary sliding is the primary deformation mechanism, as found systematically in fine-grained superplastic metals and ceramics [39,40,44, 50–53]. Inspection of Fig. 7 reveals that new and smaller-sized grains appear homogeneously distributed throughout the samples with increasing strain in the softening and steady-state stages, that is, after

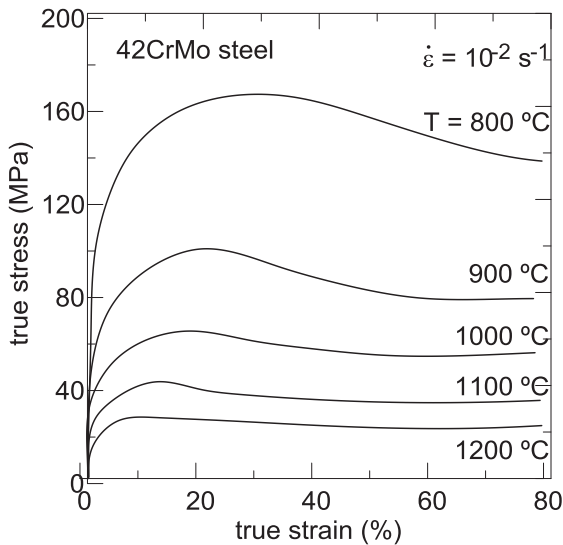


Fig. 5. Flow stress – strain curves of 42CrMo steel at constant strain rate and different temperatures [14] (with permission).

the peak stress, resulting in a refinement of the overall average grain size relative to the undeformed material. Fig. 7(d) shows the grain size distributions of the 4%- and 50%-deformed samples: at the peak stress, the average grain size $d = 0.53 \mu\text{m}$ is essentially the same as in the as-received material ($d = 0.55 \mu\text{m}$, Fig. 2(b)), while it decreases down to $d = 0.43 \mu\text{m}$ at the completion of the test. Similar results were found at other testing conditions, with grain size reductions of 15–20% after 50%-straining. Grain refinement is therefore a dynamic process that occurs progressively during softening, in agreement with the rounded shape of the stress drops.

TEM observations of strained samples (Fig. 8) have shown a high dislocation activity in the grains, particularly along and near the twin boundaries, not seen at all in the as-received material (Fig. 3). The strong interaction between dislocations and twin boundaries resulted in a progressive loss of coherence of the twin boundaries, which transformed into low-angle boundaries and finally into conventional, high angle boundaries, fragmenting the original parent grain in smaller grains. Fig. 8(c) and (d) illustrate the onset of such grain fragmentation along pre-existing twin boundaries, which finally lead to the refinement

of the grain structure. Such a dislocation-twin domain boundaries interaction was previously reported in single crystal perovskite CaTiO_3 deformed 2% along the $\langle 110 \rangle$ direction at a temperature of $1200 \text{ }^\circ\text{C}$ [31]. Compared to metals, the twin boundaries in the present material play a similar, though not identical, role to the dislocation subwalls developed in the volume of the grains during the hardening stage.

4. Discussion

The mechanical and microstructural features found in the high-temperature plastic deformation of 5Y-BCO are qualitatively identical to those found in metals and metallic alloys exhibiting continuous DRX. In these materials, the microscopic mechanisms of DRX have been exhaustively detailed in the literature [1–14]. Briefly, dislocations multiply in the early stage of creep and interact with each other in crossed glide planes, forming dislocation cell structures in the volume of the grains (polygonization), which marks the onset of strain hardening. As the strain progresses, the dislocation walls gradually transform into high-angle subboundaries by dislocation absorption, which finally are detached from the parent grains, resulting in the refinement of the grain distribution and the occurrence of the peak stress and the subsequent softening and steady-state stages. In metals, the steady state is characterized by a high stress exponent n (Eq. 1), usually between 5 and 10, in agreement with theoretical models based on dislocation-mediated intragranular mechanisms [39,41]. Very interestingly, a new twinning-induced dynamic recrystallization mechanism has been proposed in various metallic materials (such as Zr and Mg alloys, austenitic Fe and titanium) as an additional source for dislocation recovery, besides the classical continuous and discontinuous DRX mechanisms [54–60]: twin boundaries in the grains actively participate in the deformation process, decreasing the overall dislocation density and finally transforming into conventional boundaries due to twin - dislocation interaction.

4.1. Single-peak stress behavior

In metals, single or multiple peak stress behaviors have been reported depending on the nature of the material and the testing conditions [1,2,7–9]. In the latter case, stress oscillations appear before reaching the final steady state, indicating that several DRX cycles occurred during deformation. To confirm that the new and finer grain size distribution was definitively established in a single cycle in the

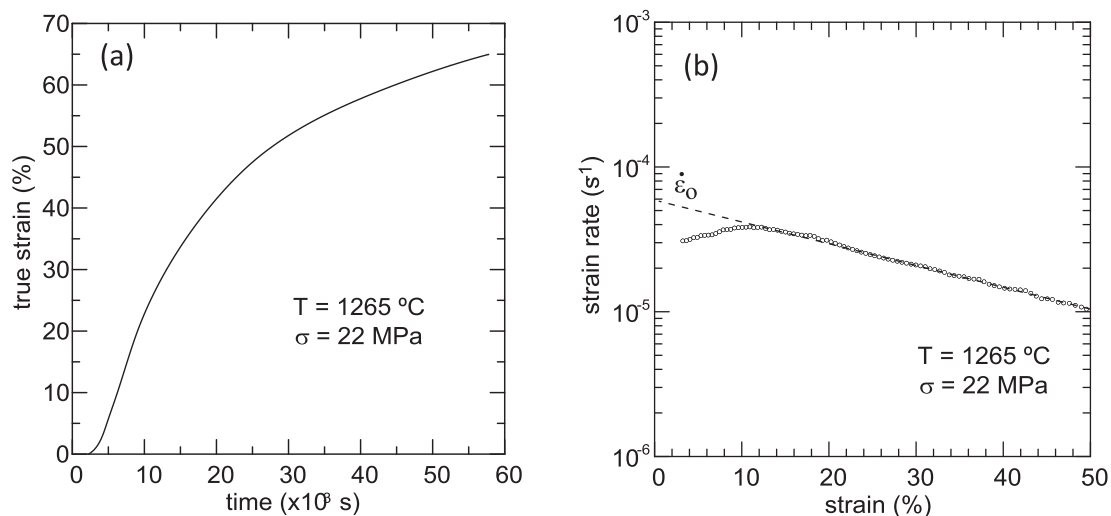


Fig. 6. Creep curve for 5Y-BCO deformed at an initial stress $\sigma = 22 \text{ MPa}$ and $T = 1265 \text{ }^\circ\text{C}$ showing the presence of the softening stage, plotted as: (a) true strain ϵ vs time t ; (b) semilog plot of strain rate $\dot{\epsilon}$ vs true strain ϵ . The constant negative slope of the $\log \dot{\epsilon} - \epsilon$ curve corresponds to a true steady state of deformation at constant load. $\dot{\epsilon}_0$ is the steady-state strain rate extrapolated to $\epsilon = 0$.

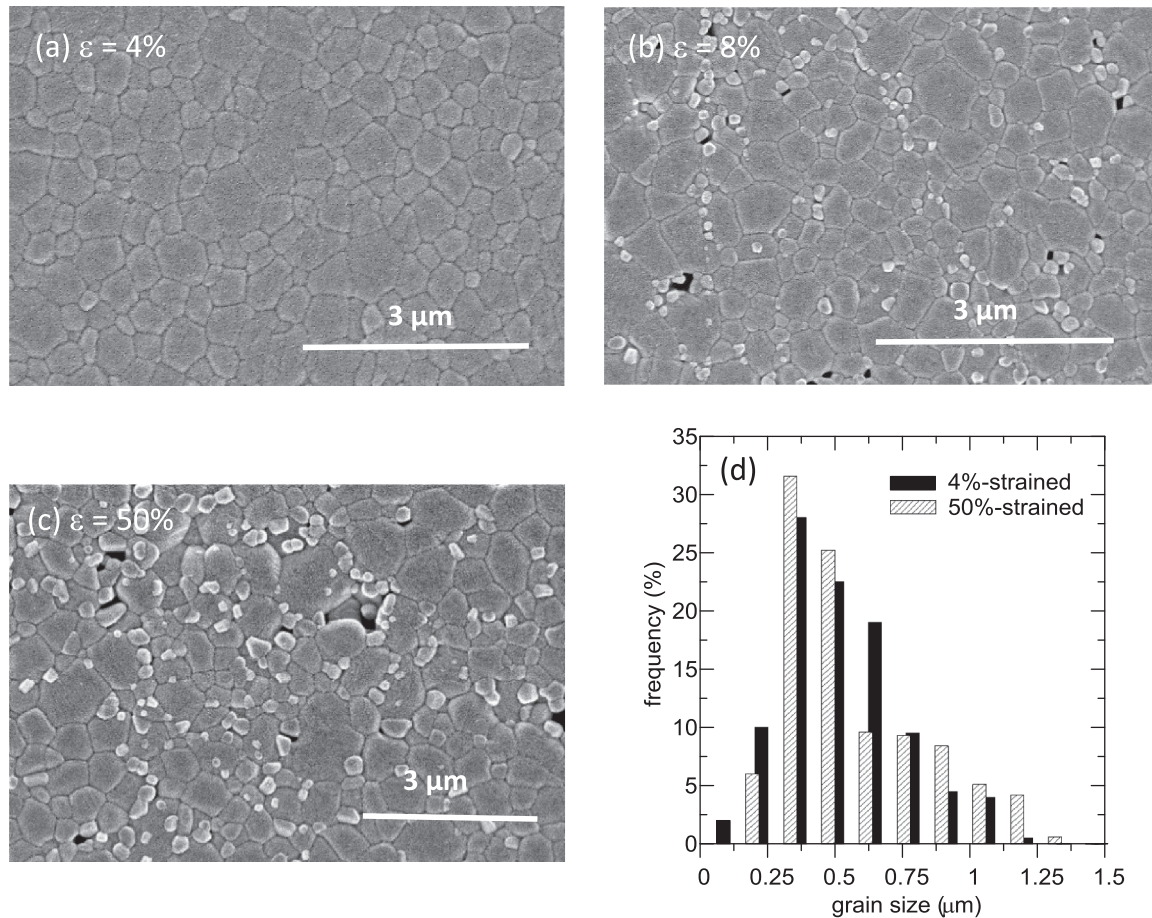


Fig. 7. Microstructure of 5Y-BCO samples deformed at $\dot{\varepsilon}_0 = 1.6 \times 10^{-4} \text{ s}^{-1}$ and $T = 1250 \text{ }^\circ\text{C}$ at different strain levels: (a) 4% (peak stress); (b) 8% (softening stage); and (c) 50% (prolonged steady-state stage). New, finer-sized grains appear after the peak stress. The grain size distributions of the 4%- and 50%-strained samples are shown in (d), with average values of 0.53 and 0.43 μm , respectively.

present perovskite, differential tests were carried out changing one variable (strain rate, temperature, or stress) during testing, as shown in Fig. 9 for an isothermal test performed at 1250 $^\circ\text{C}$ with abrupt up- and down-strain rate changes. A stress drop was observed only in the initial stage upon loading, while the other stages readily attained the stationary creep regime. It can be thus concluded that the twinning-induced grain division mechanism is mostly exhausted at the end of the softening stage.

4.2. Dynamic grain refinement by dislocation-twin boundary interaction

A plausible qualitative model is presented below (Fig. 10) that accounts for the mechanistic and microstructural features found in the perovskite oxide, based on the presence of pre-existing twin boundaries in the grains.

1. After the elastic region, grains slide on each other to accommodate the macroscopic strain by the multiplication and movement of grain boundary dislocations that comprise the structure of the boundaries, as usual in conventional (i.e., without peak stress behavior) superplastic materials [39,40,50]. Dislocations are blocked at critical points along the grain boundaries (irregularities and triple junctions), increasing the overall dislocation density and initiating the work hardening stage. In the present perovskite, intersections of pre-existing twin boundaries with grain boundaries also act as a barrier for the dislocation movement, contributing to increase the local stresses.

2. As the strain progresses, the dislocation - twin boundary interaction causes the twin boundaries with favorable orientation to accumulate dislocations, resulting in a progressive loss of their coherence. This mechanism decreases the overall density of dislocations and consequently the local stresses, marking the onset of the softening stage at a certain critical stress σ_{cr} (Fig. 4(b)). The value of σ_{cr} must be lower than the steady-state flow stress corresponding to the initial grain size d_0 , otherwise a steady state would be reached without peak stress, contrary to experimental evidence. In metals, the critical stress to initiate DRX is close to the peak stress, usually in the range $\sigma_{\text{cr}} = 0.7 - 0.9 \sigma_{\text{p}}$.
3. Upon further progress in strain, the twin boundaries gradually turn into low-angle grain boundaries and then into conventional, high-angle grain boundaries, triggering the breaking of the original grains. The continuous rotation and switching of the grains on each other allow the other grains to reach the proper orientation to initiate the fragmentation. This is a statistical process in a polycrystalline material with randomly oriented grains, giving rise to a smooth drop in flow stress.
4. Once the twinning-induced grain division is exhausted, a steady state by grain boundary sliding is established at a stress level σ_{ss} (Fig. 4(b)) corresponding to the new and finer grain distribution, according to the inverse dependence of the creep equation with grain size (Eq. (1)). In this stage, the deformation rate is then controlled by the stress restoration mechanisms operating in conventional superplastic materials (direct mass transport and/or dislocation movement along grain boundaries).

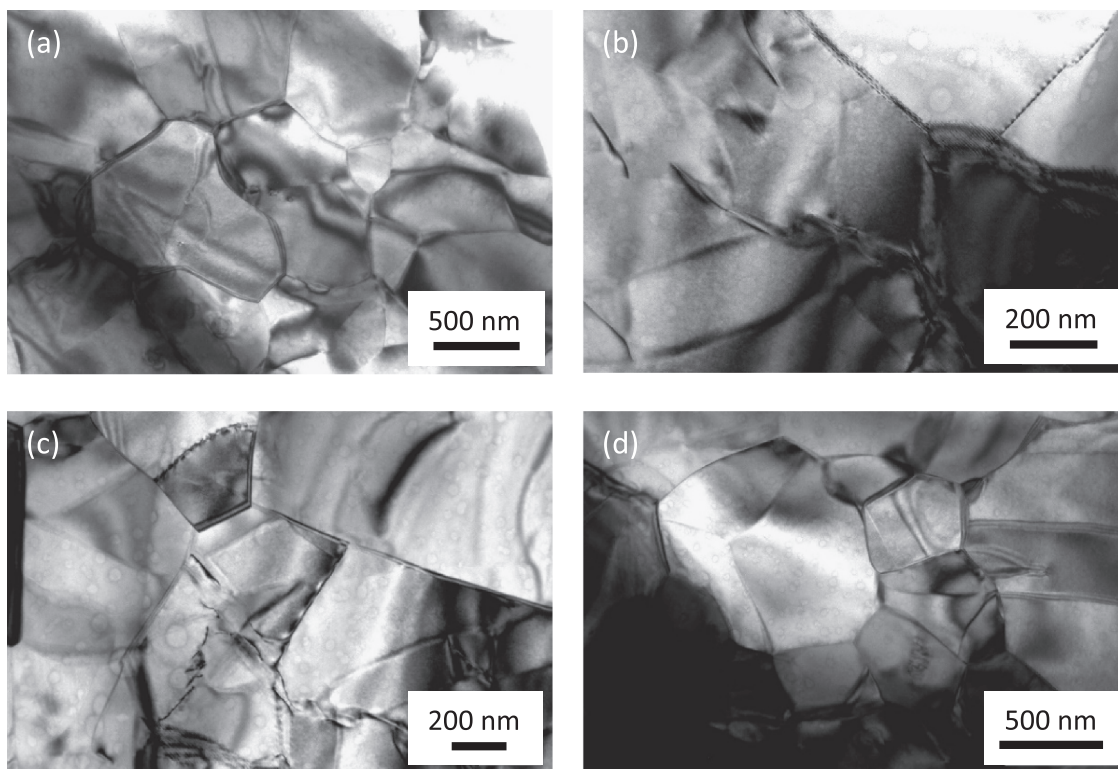


Fig. 8. Representative TEM images of 50%-strained 5Y-BCO samples showing a high dislocation activity in the grains. A strong interaction between dislocations and twin boundaries was observed, resulting in the progressive fragmentation of the original grains into new, finer grains (center of (d)).

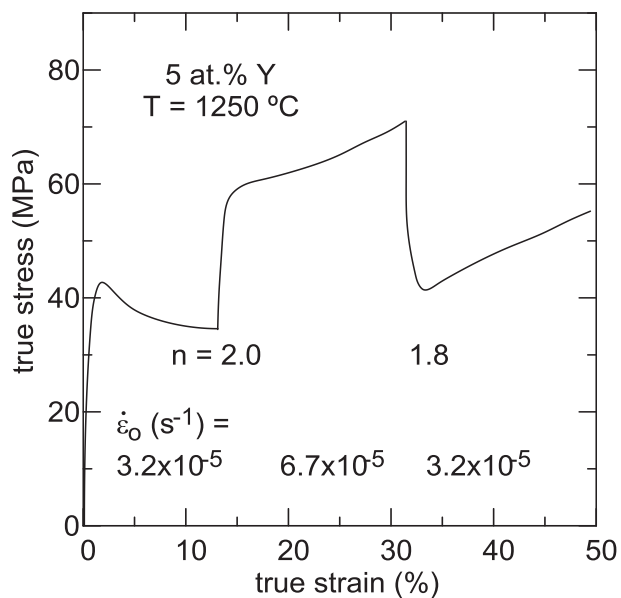


Fig. 9. Differential test with fast strain rate changes performed on 5Y-BCO at $T = 1250\text{ °C}$. Only the first stage upon loading shows a stress drop. The true stress exponent n (Eq. (1)) estimated from the changes is also shown.

4.3. Steady state of deformation

The previous discussion has shown that a true steady-state regime is definitively established (that is, at constant microstructure) after the softening transient. The stress exponent n (Eq. (1)) can be thus confidentially estimated from the steady stages of the isothermal $\sigma - \epsilon$ curves obtained at different initial deformation rates (conventional method, Fig. 4(a)). To avoid the transient softening, both σ_0 and σ_{ss} (the flow

stress extrapolated to $\epsilon = 0$ and the flow stress at the beginning of the steady state, respectively, Fig. 4(b)) have been plotted as a function of the initial strain rate $\dot{\epsilon}_0$ in Fig. 11. Both approaches yield the same stress exponent of $n = 1.9 \pm 0.1$, as expected from the good deformability of the perovskite. Alternatively, n can be estimated from strain-rate jumps during the testing of one specimen (differential method), as shown in Fig. 9, resulting in the same mean value of $n = 1.9 \pm 0.1$. This stress exponent is consistent with the values of nearly 2 systematically reported for grain boundary sliding-controlled superplasticity in fine-grained ceramics, such as 3 mol% yttria-stabilized tetragonal zirconia 3YTZP (Fig. 11, solid line) [44,51], alumina [61], alumina/zirconia composites [52], barium zirconate [45] and lanthanum silicate oxyapatite [62]. A stress exponent n of 2 is also the value predicted by most theoretical and semiphenomenological models developed to explain the superplastic behavior of fine-grained polycrystals [40] and is consistent with the absence of change in grain shape after extended secondary creep regimes. Fig. 11 also shows that the creep resistance of 5Y-BCO is similar to that of superplastic 3YTZP with the same grain size.

4.4. Analysis of peak stress

In metals, the constitutive relationship between strain rate and peak stress is commonly described by a hyperbolic sine law written as [7,13, 63]:

$$Z = \dot{\epsilon} \exp(Q_p/RT) = A [\sinh(\alpha \sigma_p)]^{n_p} \tag{2}$$

where Z is the Zener-Hollomon parameter (the temperature-compensated strain rate) and A , α , Q_p and n_p are material-dependent constants. At low stresses, Eq. (2) reduces to:

$$Z = \dot{\epsilon} \exp(Q_p/RT) = A' \sigma_p^{n_p} \tag{3}$$

which is formally identical to the power-law creep equation for steady-state deformation (Eq. (1)) but referred here to the peak stress. Typical

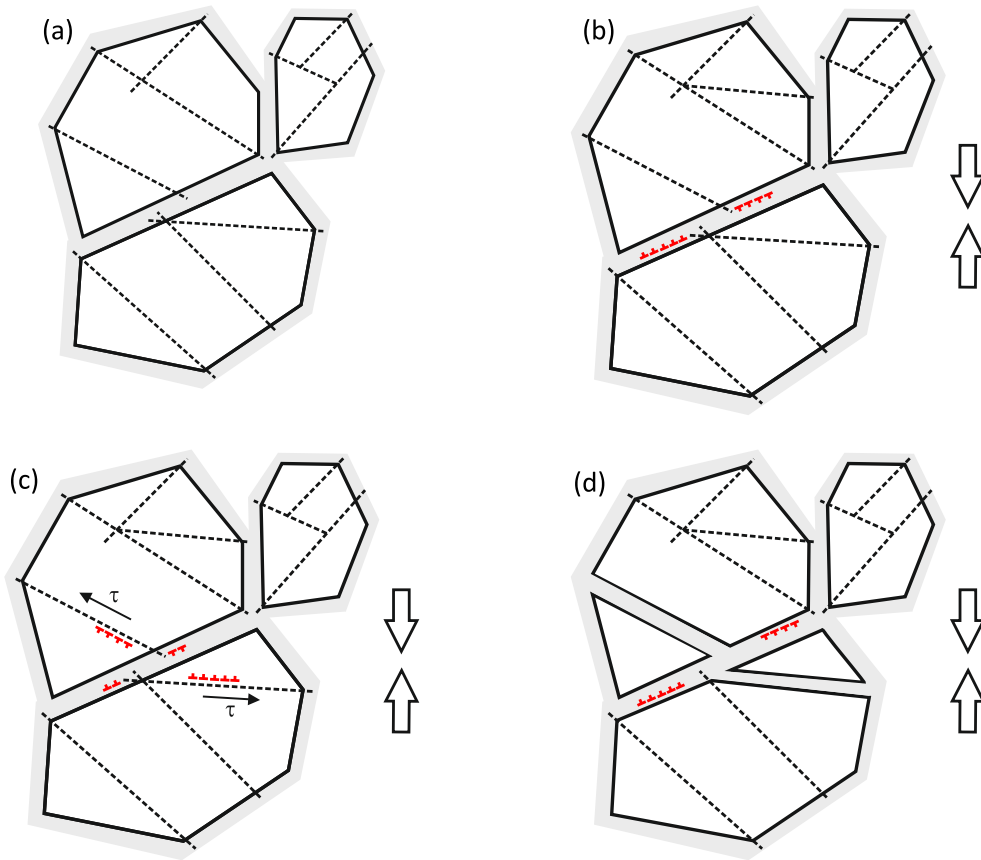


Fig. 10. Schematic diagram of the deformation mechanism proposed to explain the peak stress behavior exhibited by 5Y-BCO: (a) Initial state at $\epsilon = 0$ with pre-existing twin boundaries in the grains. (b) Dislocations multiply and move along the grain boundaries upon loading, piling up at critical points: triple junctions, intersections of twin and grain boundaries, and other irregularities (hardening stage). (c) Dislocation-twin boundary interaction decreases the local stresses, causing the onset of the softening stage. (d) As the strain proceeds, the twin boundaries gradually increase their misorientation angles and transform into conventional, high-angle boundaries, leading to the refinement of the grain structure.

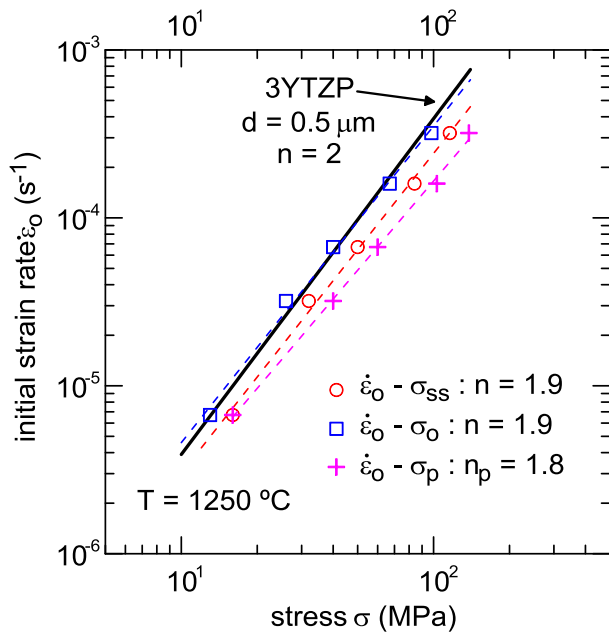


Fig. 11. Variation of the initial strain rate $\dot{\epsilon}_0$ with σ_0 (the flow stress extrapolated to $\epsilon = 0$) and with σ_{ss} (the flow stress at the beginning of the steady state) for 5Y-BCO deformed at 1250 °C (see Fig. 4(b) for nomenclature); both curves lead to the same value of the true stress exponent n (Eq. (1)). The stress coefficient n_p (Eq. (3)) obtained from the variation of $\dot{\epsilon}_0$ with peak stress σ_p (Eq. (3)) yields the same value. The creep behavior of tetragonal zirconia 3YTZP with $d = 0.5 \mu\text{m}$ [44] is displayed for reference (dashed line).

values of the stress coefficient n_p between 6 and 11 have been reported in metals, which are in the same range than the true stress exponents n for steady state [12,13,63–65]; this result indicates that the occurrence of stress peaks is also related to a dislocation-assisted deformation mechanism in these materials.

The evolution of σ_p with strain rate in 5Y-BCO has been analyzed using Eq. (3), resulting (Fig. 11):

$$\dot{\epsilon}_0 = 5.7 \times 10^{-8} \sigma_p^{1.8 \pm 0.1} \text{ (s}^{-1}\text{)} \quad (4)$$

with σ_p in MPa. The stress coefficient $n_p = 1.8 \pm 0.1$ is consistent with the true stress exponent $n = 1.9 \pm 0.1$ found in steady state, in agreement with the results in metals, and suggests again that the peak stress in the current material is not related to a dislocation recovery-controlled creep mechanism, which requires the establishment of dislocation subwalls in the volume of the grains prior to softening. Furthermore, the relationship between peak stress and peak strain can be adequately expressed by a simple linear regression equation (dashed line in Fig. 4 (a)):

$$\epsilon_p = 0.019 \sigma_p + 1.5 \text{ (\%)} \quad (5)$$

(con σ_p en MPa), as found in metals with DRX [7,9,66].

4.5. Numerical simulation of the strain – stress curves with peak stress behavior

The previous equations allow to compute numerically the stress – strain curves with peak behavior for 5Y-BCO, as shown in Fig. 12 for various initial strain rates at 1250 °C. It has been assumed that the steady state (Eq. (1)) is characterized by $A \cdot \exp(-Q/RT) = 3 \times 10^{-9}$ (in appropriate units), a stress exponent $n = 2$ and a grain size exponent $p = 2$, which is intermediate between the values reported for grain boundary sliding in ceramics [40,42,44,53,61]; in fact, the curves are

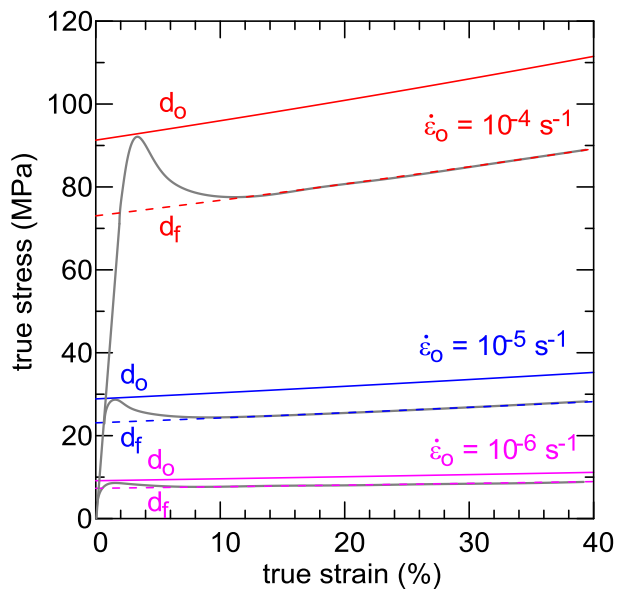


Fig. 12. True stress - true strain curves for 5Y-BCO at 1250 °C and various initial strain rates obtained using Eqs. (1)–(5). For each strain rate, two grain sizes have been plotted: $d_o = 0.5 \mu\text{m}$ (as-received value, solid lines) and $d_f = 0.4 \mu\text{m}$ (refined value, dashed lines). A 20%-reduction in grain size (as experimentally found) accounts for the observed $\sigma - \epsilon$ curves.

very little affected by the choice of p due to the small variation of about 20% in grain size during testing. Eqs. (4) and (5) have been used for the peak stress and strain, respectively.

For each strain rate, two curves have been plotted in Fig. 12, corresponding to the initial grain size $d_o = 0.5 \mu\text{m}$ (solid lines) and the final grain size $d_f = 0.4 \mu\text{m}$ (slashed lines). It can be seen that the curves correctly reproduce the experimental results, in particular the apparent loss of peak stress with decreasing strain rate and the increase of the $\sigma - \epsilon$ slope in steady state when increasing the strain rate.

5. Conclusions

Fine-grained 5 at% yttrium-doped barium cerate polycrystals have been fabricated by a conventional sintering route. XRD analyzes detected the presence of the single Pnma perovskite phase. The microstructure is formed by fine and equiaxed grains with an average grain size of $0.55 \mu\text{m}$. TEM observations have shown that the grains are well faceted and free of secondary phases and dislocations, with extensive phase transformation-induced twinning owing to the various changes in crystal structure that occur upon cooling from the sintering temperature.

Compressive mechanical tests performed at constant initial strain rate at 1200–1300 °C have shown the presence of an initial peak stress followed by a gentle softening stage and then by an extended steady state of deformation. The peak stress and the corresponding peak strain increase with increasing the initial strain rate. These experimental features are characteristics of metals that exhibit dynamic recrystallization during creep. Microstructural observations by SEM and TEM have shown that the grain size distribution is progressively refined with increasing strain after the peak stress due to the strong interaction between dislocations and pre-existing twin boundaries, which gradually transform into low-angle boundaries and then into conventional high-angle boundaries, fragmenting the original grains. The empirical equations used in metals to describe the relationships between strain rate, peak stress, and peak strain have been shown to be also valid in the present ceramic material. After the softening stage, the grain division is mostly exhausted and extended steady states of deformation are attained at constant microstructure. The stress exponent n of nearly 2 found in this regime, along with the absence of modifications in grain shape after

50%-straining, indicate that deformation is achieved primarily by grain boundary sliding, as found in other fine-grained superplastic ceramics.

Declaration of Competing Interest

The authors declare that they have no known competing financial interests or personal relationships that could have appeared to influence the work reported in this paper.

Acknowledgments

This work was supported by Project no. MAT2009-13979-C03-01, Ministerio de Ciencia e Innovación, Spain. The assistance provided by Ms. Cristina Vaquero is greatly appreciated.

References

- [1] T. Sakai, J.J. Jonas, Overview no. 35 dynamic recrystallization: mechanical and microstructural considerations, *Acta Metall.* 32 (1984) 189–209, [https://doi.org/10.1016/0001-6160\(84\)90049-X](https://doi.org/10.1016/0001-6160(84)90049-X).
- [2] T. Sakai, A. Belyakov, R. Kaibyshev, H. Miura, J.J. Jonas, Dynamic and post-dynamic recrystallization under hot, cold and severe plastic deformation conditions, *Prog. Mater. Sci.* 60 (2014) 130–207, <https://doi.org/10.1016/j.pmatsci.2013.09.002>.
- [3] H. Yu Wu, J. Chen Yang, J. hao Liao, F. jun Zhu, Dynamic behavior of extruded AZ61 Mg alloy during hot compression, *Mater. Sci. Eng. A* 535 (2012) 68–75, <https://doi.org/10.1016/j.msea.2011.12.043>.
- [4] S. Gourdet, F. Montheillet, An experimental study of the recrystallization mechanism during hot deformation of aluminium, *Mater. Sci. Eng. A* 283 (2000) 274–288, [https://doi.org/10.1016/S0921-5093\(00\)00733-4](https://doi.org/10.1016/S0921-5093(00)00733-4).
- [5] S. Gourdet, F. Montheillet, A model of continuous dynamic recrystallization, *Acta Mater.* 51 (2003) 2685–2699, [https://doi.org/10.1016/S1359-6454\(03\)00078-8](https://doi.org/10.1016/S1359-6454(03)00078-8).
- [6] T. Sakai, H. Miura, A. Goloborodko, O. Sitdikov, Continuous dynamic recrystallization during the transient severe deformation of aluminum alloy 7475, *Acta Mater.* 57 (2009) 153–162, <https://doi.org/10.1016/j.actamat.2008.09.001>.
- [7] H.J. McQueen, N.D. Ryan, Constitutive analysis in hot working, *Mater. Sci. Eng. A* 322 (2002) 43–63, [https://doi.org/10.1016/S0921-5093\(01\)01117-0](https://doi.org/10.1016/S0921-5093(01)01117-0).
- [8] K. Graetz, C. Miessen, G. Gottstein, Analysis of steady-state dynamic recrystallization, *Acta Mater.* 67 (2014) 58–66, <https://doi.org/10.1016/j.actamat.2013.12.005>.
- [9] G. Varela-Castro, J.M. Cabrera, J.M. Prado, Critical strain for dynamic recrystallisation. The particular case of steels, *Metals* 10 (2020) 135, <https://doi.org/10.3390/MET10010135>.
- [10] O. Sitdikov, R. Kaibyshev, Dynamic recrystallization in pure magnesium, *Mater. Trans.* 42 (2001) 1928–1937, <https://doi.org/10.2320/matertrans.42.1928>.
- [11] Q. Guo, D. Li, S. Guo, H. Peng, J. Hu, The effect of deformation temperature on the microstructure evolution of Inconel 625 superalloy, *J. Nucl. Mater.* 414 (2011) 440–450, <https://doi.org/10.1016/j.jnucmat.2011.05.029>.
- [12] Y.C. Lin, M.S. Chen, J. Zhong, Prediction of 42CrMo steel flow stress at high temperature and strain rate, *Mech. Res. Commun.* 35 (2008) 142–150, <https://doi.org/10.1016/j.mechrescom.2007.10.002>.
- [13] J. Liu, Z. Cui, C. Li, Modelling of flow stress characterizing dynamic recrystallization for magnesium alloy AZ31B, *Comput. Mater. Sci.* 41 (2008) 375–382, <https://doi.org/10.1016/j.commatsci.2007.04.024>.
- [14] H. Ji, H. Duan, Y. Li, W. Li, X. Huang, W. Pei, Y. Lu, Optimization the working parameters of as-forged 42CrMo steel by constitutive equation-dynamic recrystallization equation and processing maps, *J. Mater. Res. Technol.* 9 (2020) 7210–7224, <https://doi.org/10.1016/j.jmrt.2020.04.078>.
- [15] M.A. Lopez-Sanchez, A. Tommasi, W. Ben Ismail, F. Barou, Dynamic recrystallization by subgrain rotation in olivine revealed by electron backscatter diffraction, *Tectonophysics* 815 (2021), 228916, <https://doi.org/10.1016/J.TECTO.2021.228916>.
- [16] J.P. Poirier, A. Nicolas, Deformation-induced recrystallization due to progressive misorientation of subgrains, with special reference to mantle peridotites, *J. Geol.* 83 (1975) 707–720, <https://doi.org/10.1086/628163>.
- [17] S.M. Schmid, M.S. Paterson, J.N. Boland, High temperature flow and dynamic recrystallization in carrara marble, *Tectonophysics* 65 (1980) 245–280, [https://doi.org/10.1016/0040-1951\(80\)90077-3](https://doi.org/10.1016/0040-1951(80)90077-3).
- [18] P.D. Tungatt, F.J. Humphreys, The plastic deformation and dynamic recrystallization of polycrystalline sodium nitrate, *Acta Metall.* 32 (1984) 1625–1635, [https://doi.org/10.1016/0001-6160\(84\)90221-9](https://doi.org/10.1016/0001-6160(84)90221-9).
- [19] G. Hirth, J. Tullis, Dislocation creep regimes in quartz aggregates, *J. Struct. Geol.* 14 (1992) 145–159, [https://doi.org/10.1016/0191-8141\(92\)90053-Y](https://doi.org/10.1016/0191-8141(92)90053-Y).
- [20] M. Stipp, H. Stünitz, R. Heilbronner, S.M. Schmid, Dynamic recrystallization of quartz: correlation between natural and experimental conditions, *Geol. Soc. Lond., Spec. Publ.* 200 (2002) 171–190, <https://doi.org/10.1144/GSL.SP.2001.200.01.11>.
- [21] M. Guillope, J.P. Poirier, Dynamic recrystallization during creep of single-crystalline halite: an experimental study, *J. Geophys. Res. Solid Earth* 84 (1979) 5557–5567, <https://doi.org/10.1029/JB084IB10P05557>.

- [22] O. Sitdikov, R. Kaibyshev, Dislocation glide and dynamic recrystallization in LiF single crystals, *Mater. Sci. Eng. A* 328 (2002) 147–155.
- [23] C. Vaquero-Aguilar, M.J. López-Robledo, J. Martínez-Fernández, C. Real, M. Jiménez-Melendo, High-temperature mechanical behavior of polycrystalline yttrium-doped barium cerate perovskite, *J. Eur. Ceram. Soc.* 31 (2011) 1333–1338, <https://doi.org/10.1016/j.jeurceramsoc.2010.05.023>.
- [24] C. Vaquero-Aguilar, M. Jiménez-Melendo, Characterization and creep properties of proton-conducting Yb-doped barium cerate, *J. Eur. Ceram. Soc.* 31 (2011) 2671–2676, <https://doi.org/10.1016/j.jeurceramsoc.2011.01.001>.
- [25] D. Medvedev, A. Murashkina, E. Pikalova, A. Demin, A. Podias, P. Tsiakaras, BaCeO₃: materials development, properties and application, *Prog. Mater. Sci.* 60 (2014) 72–129, <https://doi.org/10.1016/j.pmatsci.2013.08.001>.
- [26] N. Ito, Intermediate-Temperature SOFCs Using Proton-Conducting Perovskite, (2009). 273–283. https://doi.org/10.1007/978-0-387-77708-5_14.
- [27] S.Y. Cheng, N.J. Ho, H.Y. Lu, Phase-transformation-induced anti-phase boundary domains in barium cerate perovskite, *J. Am. Ceram. Soc.* 89 (2006) 3498–3506, <https://doi.org/10.1111/j.1551-2916.2006.01258.x>.
- [28] S.Y. Cheng, N.J. Ho, H.Y. Lu, Phase-transformation-induced twinning in orthorhombic BaCeO₃, *J. Am. Ceram. Soc.* 91 (2008) 2298–2303, <https://doi.org/10.1111/j.1551-2916.2008.02416.x>.
- [29] K.S. Knight, Powder neutron diffraction studies of BaCe_{0.9}Y_{0.1}O_{2.95} and BaCeO₃ at 4.2 K: A possible structural site for the proton, *Solid State Ion.* 127 (2000) 43–48, [https://doi.org/10.1016/S0167-2738\(99\)00269-6](https://doi.org/10.1016/S0167-2738(99)00269-6).
- [30] A.V. Kuzmin, V.P. Gorelov, B.T. Melekh, M. Glerup, F.W. Poulsen, Phase transitions in undoped BaCeO₃, *Solid State Ion.* 162–163 (2003) 13–22, [https://doi.org/10.1016/S0167-2738\(03\)00247-9](https://doi.org/10.1016/S0167-2738(03)00247-9).
- [31] Y. Wang, R.C. Liebermann, Electron microscopy study of domain structure due to phase transitions in natural perovskite, *Phys. Chem. Miner.* 20 (1993) 147–158, <https://doi.org/10.1007/BF00200117>.
- [32] B.K. Lee, Y. Il Jung, S.J.L. Kang, J. Nowotny, {111} twin formation and abnormal grain growth in barium strontium titanate, *J. Am. Ceram. Soc.* 86 (2003) 155–160, <https://doi.org/10.1111/j.1551-2916.2003.tb03294.x>.
- [33] W.L. Wang, H.Y. Lu, Twinning induced by the rhombohedral to orthorhombic phase transition in lanthanum gallate (LaGaO₃), *Phys. Chem. Miner.* 33 (2006) 435–444, <https://doi.org/10.1007/s00269-006-0091-0>.
- [34] W.L. Wang, H.Y. Lu, Phase-transformation-induced twinning in orthorhombic LaGaO₃: {121} and {010} twins, *J. Am. Ceram. Soc.* (2006) 281–291, <https://doi.org/10.1111/j.1551-2916.2005.00673.x>.
- [35] S. Pramanik, K. Ravikumar, R. Kalsar, S. Suwas, B. Basu, On the orientation relationships in phase transformation of CaTiO₃, *Ceram. Int.* 45 (2019) 12509–12515, <https://doi.org/10.1016/J.CERAMINT.2019.03.186>.
- [36] K.H. Ryu, S.M. Haile, Chemical stability and proton conductivity of doped BaCeO₃-BaZrO₃ solid solutions, *Solid State Ion.* 125 (1999) 355–367, [https://doi.org/10.1016/S0167-2738\(99\)00196-4](https://doi.org/10.1016/S0167-2738(99)00196-4).
- [37] M. Amsif, D. Marrero-López, A. Magrasó, J. Peña-Martínez, J.C. Ruiz-Morales, P. Núñez, Synthesis and characterization of BaCeO₃-based proton conductors obtained from freeze-dried precursors, *J. Eur. Ceram. Soc.* 29 (2009) 131–138, <https://doi.org/10.1016/J.JEURCERAMSOC.2008.06.001>.
- [38] S. Yamanaka, M. Fujikane, T. Hamaguchi, H. Muta, T. Oyama, T. Matsuda, S. I. Kobayashi, K. Kurosaki, Thermophysical properties of BaZrO₃ and BaCeO₃, *J. Alloy. Compd.* 359 (2003) 109–113, [https://doi.org/10.1016/S0925-8388\(03\)00214-7](https://doi.org/10.1016/S0925-8388(03)00214-7).
- [39] J.-P. Poirier, *Creep of Crystals*, Cambridge University Press, 1985, <https://doi.org/10.1017/CBO9780511564451>.
- [40] T.G. Nieh, J. Wadsworth, O.D. Sherby, *Superplasticity in Metals and Ceramics*, Cambridge University Press, 1997, <https://doi.org/10.1017/CBO9780511525230>.
- [41] T. Bretheau, J. Castaing, J. Rabier, P. Veyssi re, Dislocation motion and high temperature plasticity of binary and ternary oxides, *Adv. Phys.* 28 (1979) 829–834, <https://doi.org/10.1080/00018737900101455>.
- [42] J. Cho, C.M. Wang, H.M. Chan, J.M. Rickman, M.P. Harmer, Role of segregating dopants on the improved creep resistance of aluminum oxide, *Acta Mater.* 47 (1999) 4197–4207, [https://doi.org/10.1016/S1359-6454\(99\)00278-5](https://doi.org/10.1016/S1359-6454(99)00278-5).
- [43] J.P. Buban, K. Matsunaga, J. Chen, N. Shibata, W.Y. Ching, T. Yamamoto, Y. Ikuhara, Grain boundary strengthening in alumina by rare earth impurities, *Science* 311 (2006) 212–215, <https://doi.org/10.1126/science.1119839>.
- [44] M. Jiménez-Melendo, A. Domínguez-Rodríguez, A. Bravo-León, Superplastic flow of fine-grained yttria-stabilized zirconia polycrystals: constitutive equation and deformation mechanisms, *J. Am. Ceram. Soc.* 81 (1998) 2761–2776, <https://doi.org/10.1111/j.1551-2916.1998.tb02695.x>.
- [45] D. Ciria, M. Jiménez-Melendo, V. Aubin, G. Dezanneau, High-temperature mechanical behavior of proton-conducting yttrium-doped barium zirconate perovskite, *J. Eur. Ceram. Soc.* 41 (2021) 1374–1383, <https://doi.org/10.1016/j.jeurceramsoc.2020.09.069>.
- [46] H.I. Yoon, D.K. Lee, H. Bin Bae, G.Y. Jo, H.S. Chung, J.G. Kim, S.J.L. Kang, S. Y. Chung, Probing dopant segregation in distinct cation sites at perovskite oxide polycrystal interfaces, *Nat. Commun.* 8 (2017) 1–8, <https://doi.org/10.1038/s41467-017-01134-x>.
- [47] K. Morita, B.-N. Kim, K. Hiraga, Y. Sakka, Yield drop in high-strain-rate superplastic deformation of ZrO₂-30 vol% MgAl₂O₄ spinel composite, *Philos. Mag. Lett.* 83 (2003) 533–541, <https://doi.org/10.1080/09500830310001597018>.
- [48] P.C. DOKKO, J.A. PASK, High-temperature stress-strain behavior of MgO in compression, *J. Am. Ceram. Soc.* 62 (1979) 433–439, <https://doi.org/10.1111/j.1151-2916.1979.tb19099.x>.
- [49] G. DAS, K.S. MAZDIYASNI, H.A. LIPSITT, Mechanical properties of polycrystalline TiC, *J. Am. Ceram. Soc.* 65 (1982) 104–110, <https://doi.org/10.1111/j.1151-2916.1982.tb10366.x>.
- [50] E. Alabort, P. Kontis, D. Barba, K. Dragnevski, R.C. Reed, On the mechanisms of superplasticity in Ti-6Al-4V, *Acta Mater.* 105 (2016) 449–463, <https://doi.org/10.1016/j.actamat.2015.12.003>.
- [51] F. WAKAI, S. SAKAGUCHI, Y. MATSUNO, Superplasticity of yttria-stabilized tetragonal ZrO₂ polycrystals, *Adv. Ceram. Mater.* 1 (1986) 259–263, <https://doi.org/10.1111/j.1551-2916.1986.tb00026.x>.
- [52] F. WAKAI, H. KATO, Superplasticity of TZP/Al₂O₃ composite, *Adv. Ceram. Mater.* 3 (1988) 71–76, <https://doi.org/10.1111/j.1551-2916.1988.tb00173.x>.
- [53] L. Clarisse, R. Baddi, A. Bataille, J. Crampon, R. Duclos, J. Vicens, Superplastic deformation mechanisms during creep of alumina-zirconia composites, *Acta Mater.* 45 (1997) 3843–3853, [https://doi.org/10.1016/S1359-6454\(97\)89771-6](https://doi.org/10.1016/S1359-6454(97)89771-6).
- [54] S. Li, B. Luan, L. Chu, X. Zhang, G. Yuan, R. Liu, K.L. Murty, Q. Liu, Twinning behaviors and grain refinement mechanisms during friction stir processing of Zr alloy, *Mater. Charact.* 163 (2020), 110277, <https://doi.org/10.1016/j.matchar.2020.110277>.
- [55] W. Chen, C. Jia, B. Hu, C. Zheng, D. Li, Evolution of twins and sub-boundaries at the early stage of dynamic recrystallization in a Ni-30%Fe austenitic model alloy, *Mater. Sci. Eng. A* 733 (2018) 419–428, <https://doi.org/10.1016/j.msea.2018.07.071>.
- [56] C.K. Yan, A.H. Feng, S.J. Qu, G.J. Cao, J.L. Sun, J. Shen, D.L. Chen, Dynamic recrystallization of titanium: effect of pre-activated twinning at cryogenic temperature, *Acta Mater.* 154 (2018) 311–324, <https://doi.org/10.1016/j.actamat.2018.05.057>.
- [57] Q. Ma, B. Li, E.B. Marin, S.J. Horstemeyer, Twinning-induced dynamic recrystallization in a magnesium alloy extruded at 450 °C, *Scr. Mater.* 65 (2011) 823–826, <https://doi.org/10.1016/j.scriptamat.2011.07.046>.
- [58] H. Beladi, P. Cizek, P.D. Hodgson, Dynamic recrystallization of austenite in Ni-30 Pct Fe model alloy: microstructure and texture evolution, *Metall. Mater. Trans. A* 40 (2009) 1175–1189, <https://doi.org/10.1007/S11661-009-9799-Z>.
- [59] Z. Yu, H. Choo, Influence of twinning on the grain refinement during high-temperature deformation in a magnesium alloy, *Scr. Mater.* 64 (2011) 434–437, <https://doi.org/10.1016/J.SCRIPTAMAT.2010.11.009>.
- [60] O. Sitdikov, R. Kaibyshev, T. Sakai, Dynamic recrystallization based on twinning in coarse-grained Mg, *Mater. Sci. Forum* (2003) 521–526, <https://doi.org/10.4028/www.scientific.net/msf.419-422.521>.
- [61] F. Wakai, T. Nagano, T. Iga, Hardening in creep of alumina by zirconium segregation at the grain boundary, *J. Am. Ceram. Soc.* 80 (1997) 2361–2366, <https://doi.org/10.1111/j.1151-2916.1997.tb03128.x>.
- [62] D. Ciria, M. Jiménez-Melendo, V. Aubin, G. Dezanneau, Creep properties of high dense La_{0.33}Si_{0.26}O₂₆ electrolyte for SOFCs, *J. Eur. Ceram. Soc.* 40 (2020) 1989–1998, <https://doi.org/10.1016/j.jeurceramsoc.2020.01.004>.
- [63] L. Wang, F. Liu, J.J. Cheng, Q. Zuo, C.F. Chen, Hot deformation characteristics and processing map analysis for Nickel-based corrosion resistant alloy, *J. Alloy. Compd.* 623 (2015) 69–78, <https://doi.org/10.1016/J.JALLCOM.2014.10.034>.
- [64] S. Solhjo, Determination of critical strain for initiation of dynamic recrystallization, *Mater. Des.* 31 (2010) 1360–1364, <https://doi.org/10.1016/j.matdes.2009.09.001>.
- [65] S. Solhjo, Analysis of flow stress up to the peak at hot deformation, *Mater. Des.* 30 (2009) 3036–3040, <https://doi.org/10.1016/j.matdes.2008.12.014>.
- [66] E. Evangelista, M. Masini, M. El Mehtedi, S. Spigarelli, Hot working and multipass deformation of a 41Cr4 steel, *J. Alloy. Compd.* 378 (2004) 151–154, <https://doi.org/10.1016/J.JALLCOM.2003.11.170>.